Journal of Computational Physics 270 (2014) 640–659

Contents lists available at ScienceDirect

Journal of Computational Physics

www.elsevier.com/locate/jcp

Hybrid immersed interface-immersed boundary methods for AC dielectrophoresis

Mohammad Robiul Hossan [a,b], Robert Dillon [c], Prashanta Dutta [a,*]

[a] School of Mechanical and Materials Engineering, Washington State University, Pullman, WA 99164-2920, United States
[b] Department of Engineering and Physics, University of Central Oklahoma, Edmond, OK 73034-5209, United States
[c] Department of Mathematics, Washington State University, Pullman, WA 99164-3113, United States

ARTICLE INFO

Article history:
Received 4 May 2013
Received in revised form 11 March 2014
Accepted 4 April 2014
Available online 18 April 2014

Keywords:
Dielectrophoresis
Particle assembly
Immersed interface
Immersed boundary

ABSTRACT

Dielectrophoresis, a nonlinear electrokinetic transport mechanism, has become popular in many engineering applications including manipulation, characterization and actuation of biomaterials, particles and biological cells. In this paper, we present a hybrid immersed interface–immersed boundary method to study AC dielectrophoresis where an algorithm is developed to solve the complex Poisson equation using a real variable formulation. An immersed interface method is employed to obtain the AC electric field in a fluid media with suspended particles and an immersed boundary method is used for the fluid equations and particle transport. The convergence of the proposed algorithm as well as validation of the hybrid scheme with experimental results is presented. In this paper, the Maxwell stress tensor is used to calculate the dielectrophoretic force acting on particles by considering the physical effect of particles in the computational domain. Thus, this study eliminates the approximations used in point dipole methods for calculating dielectrophoretic force. A comparative study between Maxwell stress tensor and point dipole methods for computing dielectrophoretic forces are presented. The hybrid method is used to investigate the physics of dielectrophoresis in microfluidic devices using an AC electric field. The numerical results show that with proper design and appropriate selection of applied potential and frequency, global electric field minima can be obtained to facilitate multiple particle trapping by exploiting the mechanism of negative dielectrophoresis. Our numerical results also show that electrically neutral particles form a chain parallel to the applied electric field irrespective of their initial orientation when an AC electric field is applied. This proposed hybrid numerical scheme will help to better understand dielectrophoresis and to design and optimize microfluidic devices.

© 2014 Elsevier Inc. All rights reserved.

1. Introduction

Dielectrophoretic particle transport in microfluidic devices has become very popular in many applications including the manipulation, characterization, and actuation of micro/nano particles and biological cells. At the same time there is rapidly growing interest in understanding the underlying multiphysics of this complex phenomena [1–3]. Precise control and manipulation of the nonlinear dielectrophoretic force field facilitates cell trapping, cell characterization, and cell separation. The dynamics of dielectrophoresis has been studied using dipole approximations [1,4,5]. The dipole approximation, popularly

* Corresponding author. Tel.: +1 509 3357989; fax: +1 509 3354662.
E-mail address: dutta@mail.wsu.edu (P. Dutta).

http://dx.doi.org/10.1016/j.jcp.2014.04.012
0021-9991/© 2014 Elsevier Inc. All rights reserved.

known as the point dipole method (PD) or effective dipole moment (EDM), provides good estimations of dielectrophoretic forces in some cases. However, it loses validity and can produce erroneous result if (i) the particles or cells are near an electrode and/or the spatial non-uniformity of the electric field is very high [6], (ii) two or more particles are close to each other or clustered together [7], (iii) a particle is large compared to the length scale of the device or computational domain [8], and (iv) particles have very complex geometries or are deformable [9]. It has been suggested [6,10] to use higher order approximation such as quadrapole instead of dipole to improve the estimation of the dielectrophoretic force. However, it cannot completely eliminate the inaccuracy as the higher order terms are still calculated based on the electric field without considering the effect of the particle on the electric field [11]. Particles create significant spatial nonuniformities in the electric field. Particle induced nonuniformity can be the fundamental reason for dielectrophoretic particle assembly or dielectrophoretic colloidal particle aggregation [12]. Thus it is very important to accurately calculate the electric field distribution for applications such as particle assembly where the nonuniformities in electric field are caused by the effect of finite sized particles or cells. Once the electric field is calculated, the Maxwell stress tensor (MST) can be used to calculate the dielectrophoretic force acting on particles.

The challenge of the MST approach is to include the physical effects of finite sized particle in the numerical scheme and solve the problem efficiently with a reasonable computational cost. Recently several MST based dielectrophoresis studies have been reported using finite element methods with an arbitrary Lagrangian–Eulerian (ALE) algorithm [13]. In general, finite element methods require a high-resolution mesh when particles are close to each other or near an electrode. Moreover, the ALE algorithm requires moving mesh to update the particle locations. Recently Bhalla et al. [14] presented an immersed electrohydrodynamics method for fluid structure interactions, to study cell separation, free swimming, nanowire assembly, electrolocation, and dielectrophoresis, where the body force is calculated from the Maxwell stress tensor [15]. They used a fixed Eulerian grid with local adaptive mesh refinement. Al-Jarro et al. [16] reported an MST based finite volume method for predicting dielectrophoretic particle trajectory. However the model employed a simple Stokes drag force expression for hydrodynamic effect. Moreover, in that study elastic deformations, particle dynamics and particle–fluid interactions were not considered. Le et al. [17] provided a coupled immersed interface–boundary element method for dielectrophoretic particle trapping where the electric field was obtained by a boundary element method, and the viscous fluid flow problem was solved with an immersed interface method. The boundary element method usually provides fully populated matrices and is not convenient for large systems. Liu et al. [9] presented an immersed electrokinetic finite element method for electrokinetic problems where both electric field and fluid flow were solved using finite element methods. All of the aforementioned methods solved the complex variable formulation of electric potential for AC dielectrophoresis using matrix operations with complex variables. Generally, manipulation of complex numbers and matrix operation of complex variables are not computationally efficient [18].

In this paper we present an alternative algorithm that decouples the complex variable partial differential equation (PDE) for the electric potential into two sets of real valued PDEs. The coupling between these two equations appears as an interface jump conditions across the embedded particles' surface. We propose a hybrid immersed interface–immersed boundary, an interface-resolved nonbody-fitted grid method to capture the underlying multiphysics phenomena of dielectrophoresis. The immersed interface method [19] is used to solve the decoupled equations for obtaining the complex electric field distribution. The immersed interface method developed by Li et al. [20] is generalized for AC dielectrophoresis and modified to obtain solution of the electric potential with multiple suspended particles in the fluid media. The strong discontinuity on the interface is captured in the immersed interface method by using an augmented interpolation scheme with correction term. The use of IIM in this hybrid method provides second order accuracy of electric field calculation which is lacking in the existing numerical method for electrohydrodynamic model [14]. We used the immersed boundary method to model particle driven fluid flow. This method has been demonstrated to be stable, efficient and accurate for fluid flow with particle–fluid interaction, especially in biological applications with moving inner boundaries [21–23]. The hydrodynamic forces due to particle–fluid interactions are obtained through contribution from the bending, tethering and elastic deformation of the particles. *This proposed hybrid method eliminates the need for dipole and quadruple approximations that are currently used in dielectrophoresis analysis and provides an alternative efficient numerical scheme.*

The remainder of the paper is organized as follows. In Section 2, we describe the theory of dielectrophoresis with relevant governing equations and boundary conditions. The decoupled complex variable equations for the electric potential are presented. The strategy of calculating dielectrophoresis without boundary integration and full domain concept are introduced as well. In Section 3, we describe the numerical methods used in this study. First, an algorithm is introduced to solve decoupled real valued equations for AC potential. Next, we describe the formulation of the immersed interface method and a solution strategy for the discrete equations. We also review the immersed boundary method for solving the Navier–Stokes equations for fluid flow. Here we provide the details of computing the Eulerian forcing terms due to the deformation of elastic particle. This is followed by a brief step by step description of the hybrid algorithm. In Section 4, we present our numerical results and discussion. We begin with convergence studies of the decoupled algorithm, the immersed interface method, and the immersed boundary method. The numerical code is validated by comparison with a set of reported experimental results. We also present a comparative study to elucidate the difference between the MST and point dipole methods for computing dielectrophoretic force. In Section 5, we present three different applications of dielectrophoresis to illustrate the flexibility of our numerical scheme. The physics of dielectrophoresis is discussed with a simple microfluidic configuration, a design of dielectrophoretic multiple particle trapping is investigated and discussed, and the mechanism of

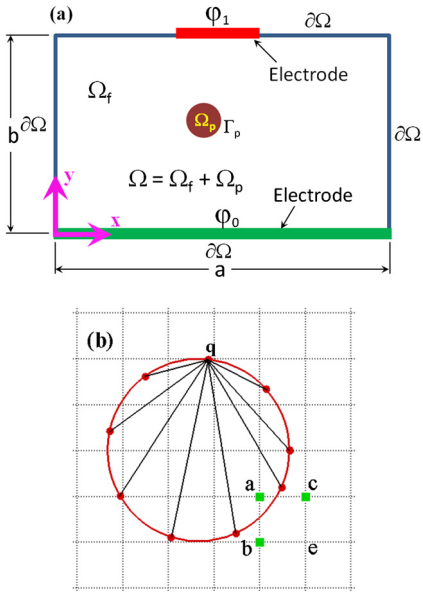

Fig. 1. (a) A typical computational domain Ω to develop a mathematical model for dielectrophoretic phenomena with an embedded particle. Particle boundary is denoted with Γ_p while computational domain boundaries are denoted with $\partial\Omega$. A pole electrode is placed at the top surface, while a plate electrode is on the bottom surface. A square AC electric potential is applied on each electrode with a peak to peak potential difference V_{p-p}, frequency f, and a phase angle β. (b) Illustration of irregular grids [■] and elastic links of an immersed boundary point 'q' to the rest of the immersed boundary points 'd' [$d \neq q$] of an embedded particle boundary in the immersed interface–immersed boundary method.

dielectrophoretic particle assembly is demonstrated. Finally, brief summary and concluding remarks are provided in Section 6.

2. Theory

The physics of dielectrophoresis can be attributed to the interaction between a nonuniform electric field and polarizable particles or entities suspended in a fluid media. The distinct feature of this phenomenon is that it is equally applicable to charged and neutral particles or cells. In presence of an electric field, accumulation of induced charge, also known as polarization, appears at the interface between particles and suspending media due to the dielectric properties. This charge accumulation creates an induced electric dipole, by inducing a net positive charge on one side and a net negative charge on the other side of the interface due to the variation of dielectric properties. Thus, the nonuniform external electric field creates a net force, known as dielectrophoretic (DEP) force, at the interface. Generally an AC electric potential is applied to create nonuniform electric field. AC electric field also suppresses other electrokinetic effects such as electroosmosis and electrophoresis even with charged particles. The relative polarizability of the interacting particle and suspended media sets the direction of net force. In positive DEP the particle is more polarizable than the media, and the net force drives the particles towards higher electric field region. On the other hand, in negative DEP the particle is less polarizable than the media and the DEP force moves particles toward lower electric field regions [10]. Under the action of dielectrophoresis, particles induce a flow in a stationary suspending media and modify the adjacent flow field in a moving media. Hence, dielectrophoresis creates complex interactions among the electric field, particle positions and orientations, and hydrodynamic forces.

2.1. Governing equations and boundary conditions

Based on typical applied electric potential and frequencies and interaction between electric field and hydrodynamics, dielectrophoresis can be described as a combination of a quasi-electrostatic problem and a transient particle flow problem. To develop a mathematical model, we consider a particle suspended in a domain as shown in Fig. 1(a) filled with an incompressible Newtonian viscous fluid. The particle domain is represented by Ω_p with the surface enclosed by Γ_p. The computational domain Ω is enclosed by the boundary $\partial\Omega$. Although the model is valid for any number of suspended particles, for simplicity we show only one particle and later we show results for multiple particles.

The governing equation for the complex electric potential distribution of a quasi-electrostatic problem is derived (shown in Appendix A) from Maxwell's equation as:

$$\nabla \cdot (\tilde{\varepsilon} \nabla \tilde{\varphi}) = 0 \tag{1}$$

The complex permittivity $\tilde{\varepsilon}$ and the complex potential $\tilde{\varphi}$ are given as $\tilde{\varepsilon} = \varepsilon_r - j\varepsilon_i$ and $\tilde{\varphi} = \varphi(\vec{x})e^{j\omega t}$, respectively. Here ε_r is the real part of complex permittivity, ε_i is the imaginary part, where $\varepsilon_i = \sigma/\omega$, σ is electrical conductivity, ω is angular frequency and t is time. The angular frequency ω is related to frequency f as $\omega = 2\pi f$. In a low frequency regime, electrical conductivity plays a dominant role, while in a high frequency regime, permittivity dominates. For the system shown in Fig. 1, the boundary conditions are:

$$\tilde{\varphi}(\vec{x}) = \varphi_0 e^{j\omega t} \quad \text{on an electrode surface} \tag{2a}$$

$$\frac{\partial \tilde{\varphi}(\vec{x})}{\partial \vec{x}} = 0 \quad \text{on an insulating surface} \tag{2b}$$

The continuity of the electric potential and the normal component of the electric flux density are imposed as interface conditions at a material boundary:

$$\tilde{\varphi}_p = \tilde{\varphi}_f \tag{3a}$$

$$\tilde{\varepsilon}_p \frac{\partial \tilde{\varphi}_p}{\partial \vec{n}} = \tilde{\varepsilon}_f \frac{\partial \tilde{\varphi}_f}{\partial \vec{n}} \tag{3b}$$

where subscripts p is for the particles, f is for the fluid media and $\vec{n}$ is the surface normal. The electric field $\tilde{\vec{E}}$ is assumed to be irrotational and is calculated as

$$\tilde{\vec{E}} = -\nabla\tilde{\varphi} \tag{4}$$

The viscous fluid flow is governed by the incompressible Navier–Stokes equations and continuity equation as:

$$\rho\left[\vec{u}_t + (\vec{u}\cdot\nabla)\vec{u}\right] = -\nabla p + \mu\Delta\vec{u} + \vec{F}(\vec{x},t) \tag{5}$$

$$\nabla\cdot\vec{u} = 0 \tag{6}$$

where ρ is the fluid density, $\vec{u}$ is the fluid velocity, p is the pressure and $\vec{F}$ is the body force due to the dielectrophoresis.

2.2. Decoupling of the complex electric potential equation

In a recent work, Bhalla et al. presented a similar mathematical model for electrohydrodynamics problems. In their work, the complex electrostatic equation given by (1) was expressed in terms of real variables for real and complex parts of the solution similar to Eq. (7) (shown below). They solved the resultant system of equations using a finite difference scheme with a Krylov subspace method. However, they did not include immersed interface continuity condition as shown above in Eq. (3). No special consideration was given for problems involving sharp discontinuities. Thus, although no convergence studies were shown, the solution of the electric potential was unlikely to be better than first order. In this study, our objective is to develop a computationally efficient numerical scheme for second order accurate electric potential from complex electrostatic equation (1).

In principle, the electric potential and field distribution can be obtained by solving the complex form of Maxwell's equation (Eq. (1)) using an immersed interface method (IIM) [19,20]. As an alternative to the complex formulation, in the case of piecewise constant material properties, we express governing equations as electric potential equations for the real and imaginary parts of φ with appropriate boundary and interface conditions. The advantage of this method is that one can use an existing IIM solvers. In addition, in this decoupled method, one solves two $N \times N$ problems as opposed to a $2N \times 2N$ problem. Thus potentially reducing the computational cost and requiring less memory.

For this purpose, we redefine the complex electric potential as $\tilde{\varphi} = \varphi(\vec{x})e^{j\omega t} = \varphi_r + j\varphi_i$ where the real part, $\varphi_r = \varphi\cos\omega t$, and the imaginary part, $\varphi_i = \varphi\sin\omega t$. With this definition the governing equation (1) becomes

$$\left[\nabla\cdot(\varepsilon_r\nabla\varphi_r) + \nabla\cdot(\varepsilon_i\nabla\varphi_i)\right] + j\left[\nabla\cdot(\varepsilon_r\nabla\varphi_i) - \nabla\cdot(\varepsilon_i\nabla\varphi_r)\right] = 0 \tag{7}$$

For a homogeneous fluid media and suspended particles, we consider piecewise constant dielectric properties. In other words, dielectric properties for fluid media do not vary within the fluid media and dielectric properties for a particle remain same throughout the particle domain. With piecewise constant coefficients, Eq. (7) reduces to equations of the form

$$\varepsilon_r\nabla^2\varphi_r + \varepsilon_i\nabla^2\varphi_i = 0 \tag{8a}$$

$$\varepsilon_r\nabla^2\varphi_i - \varepsilon_i\nabla^2\varphi_r = 0 \tag{8b}$$

in the fluid and particle domains where ε_r and ε_i are piecewise constant. By addition and subtraction, Eqs. (8) can be expressed as

$$\nabla^2\varphi_r = 0 \tag{9a}$$

$$\nabla^2\varphi_i = 0 \tag{9b}$$

Eqs. (9a) and (9b) must be satisfied in both particle and fluid domains. By substituting $\tilde{\varphi} = \varphi_r + j\varphi_i$, the interface conditions given by (3b) can be written as

$$\left[\left(\varepsilon_r \frac{\partial \varphi_r}{\partial n} + \varepsilon_i \frac{\partial \varphi_{i,}}{\partial n}\right) + j\left(\varepsilon_r \frac{\partial \varphi_i}{\partial n} - \varepsilon_i \frac{\partial \varphi_r}{\partial n}\right)\right]_p = \left[\left(\varepsilon_r \frac{\partial \varphi_r}{\partial n} + \varepsilon_i \frac{\partial \varphi_{i,}}{\partial n}\right) + j\left(\varepsilon_r \frac{\partial \varphi_i}{\partial n} - \varepsilon_i \frac{\partial \varphi_r}{\partial n}\right)\right]_f \tag{10}$$

By equating real and imaginary parts, we obtain the interface flux jump conditions

$$\varepsilon_{r,f} \frac{\partial \varphi_{r,f}}{\partial n} - \varepsilon_{r,p} \frac{\partial \varphi_{r,p}}{\partial n} = -\left[\varepsilon_{i,f} \frac{\partial \varphi_{i,f}}{\partial n} - \varepsilon_{i,p} \frac{\partial \varphi_{i,p}}{\partial n}\right] \tag{11a}$$

$$\varepsilon_{r,f} \frac{\partial \varphi_{i,f}}{\partial n} - \varepsilon_{r,p} \frac{\partial \varphi_{i,p}}{\partial n} = \left[\varepsilon_{i,f} \frac{\partial \varphi_{r,f}}{\partial n} - \varepsilon_{i,p} \frac{\partial \varphi_{r,p}}{\partial n}\right] \tag{11b}$$

where subscripts r represent real part; i, the imaginary part; f, the fluid media; and p, the particle media. Finally we obtain two sets of real valued governing equations with boundary and interface conditions for the complex electric potential.

For the real part of electric potential, φ_r we solve the following set of equations

$$\nabla^2 \varphi_r = 0 \tag{12}$$

with boundary conditions

$$\varphi_r(\vec{x}) = \varphi_{r,0}(\vec{x}) \quad \text{on an electrode surface} \tag{13a}$$

$$\frac{\partial \varphi_r(\vec{x})}{\partial \vec{x}} = 0 \quad \text{on an insulating surface} \tag{13b}$$

with interface conditions given by

$$\varphi_{r,p} = \varphi_{r,f} \tag{14a}$$

$$\varepsilon_{r,f} \frac{\partial \varphi_{r,f}}{\partial n} - \varepsilon_{r,p} \frac{\partial \varphi_{r,p}}{\partial n} = \chi_r(\varepsilon_i, \varphi_i) \tag{14b}$$

where $\chi_r(\varepsilon_i, \varphi_i) = -[\varepsilon_{i,f} \frac{\partial \varphi_{i,f}}{\partial n} - \varepsilon_{i,p} \frac{\partial \varphi_{i,p}}{\partial n}]$ is the flux jump for the real part of the governing equation. In Eq. (13a), the subscript 0 denotes the real component of the prescribed electric potential.

Similarly, the equation for the imaginary part φ_i is given by

$$\nabla^2 \varphi_i = 0 \tag{15}$$

with boundary conditions

$$\varphi_i(\vec{x}) = \varphi_{i,0}(\vec{x}) \quad \text{on an electrode surface} \tag{16a}$$

$$\frac{\partial \varphi_i(\vec{x})}{\partial \vec{x}} = 0 \quad \text{on an insulating surface} \tag{16b}$$

with corresponding interface conditions given by

$$\varphi_{i,p} = \varphi_{i,f} \tag{17a}$$

$$\varepsilon_{r,f} \frac{\partial \varphi_{i,f}}{\partial n} - \varepsilon_{r,p} \frac{\partial \varphi_{i,p}}{\partial n} = \chi_i(\varepsilon_i, \varphi_r) \tag{17b}$$

where $\chi_i(\varepsilon_i, \varphi_r) = [\varepsilon_{i,f} \frac{\partial \varphi_{r,f}}{\partial n} - \varepsilon_{i,p} \frac{\partial \varphi_{r,p}}{\partial n}]$ is the flux jump condition for the imaginary part of the governing equation. In Eq. (16a), the subscript 0 denotes the imaginary component of the prescribed electric potential. The equation for φ_r and φ_i are coupled through the interface condition Eqs. (14b) and (17b). We developed an iterative process to satisfy this interface condition that requires only a few iterations to converge. The details of the iteration process are discussed later in Section 3.

2.3. Calculation of dielectrophoretic force density

The electrically driven body force is the main driving mechanism in dielectrophoresis. Hence it is very important to calculate this force accurately to understand the physics and design dielectrophoretic based tools for engineering applications. The frequency for applied potentials in typical dielectrophoresis applications is below 100 MHz for which the wavelength is few meters. This is several orders of magnitude larger than the size of DEP electrodes. Hence the contribution due to the magnetic field in the Maxwell stress tensor can be neglected using a near-field approximation [11]. With this approximation

the Maxwell stress tensor for the AC electric field is given by

$$\vec{\vec{M}}_M = \frac{1}{4}\tilde{\varepsilon}\left[\left(\vec{\vec{E}}\vec{\vec{E}}^* + \vec{\vec{E}}\vec{\vec{E}}^*\right) - \left(\vec{\vec{E}}\cdot\vec{\vec{E}}^*\right)\vec{\vec{I}}\right] + \frac{1}{4}\tilde{\varepsilon}\left[\left(\vec{\vec{E}}\vec{\vec{E}} + \vec{\vec{E}}^*\vec{\vec{E}}^*\right) - \frac{1}{2}\left(\vec{\vec{E}}\cdot\vec{\vec{E}} + \vec{\vec{E}}^*\cdot\vec{\vec{E}}^*\right)\vec{\vec{I}}\right] \tag{18}$$

where $\vec{\vec{E}}(\vec{x},t) = \mathrm{Re}(\vec{E}_0(\vec{x})e^{j\omega t})$, $\vec{\vec{E}}^*$ is the conjugate of $\vec{\vec{E}}$, $\vec{\vec{I}}$ is the unit tensor, $\vec{\vec{E}}\vec{\vec{E}}^*$ is the dyadic product of electric field. The first part of Eq. (18) is the time averaged stress tensor while the second part represents the instantaneous term. The instantaneous term vanishes under time averaging. The dielectrophoretic force is calculated from the time averaged Maxwell stress tensor by integration over the period of the AC frequency of applied potential. The time scale of the dielectrophoretic motion of a particle is much larger than the time scale of the AC frequency. Hence the time averaged dielectrophoretic force density on the particle surface in Lagrangian form is given by

$$\vec{f}_{DEP} = \vec{\vec{M}}_M|_{TA}\cdot\vec{n} = \left(\frac{1}{T}\int_0^T \vec{\vec{M}}_M dt\right)\cdot\vec{n} = \frac{1}{4}\mathrm{Re}(\tilde{\varepsilon})\left[\left(\vec{\vec{E}}\vec{\vec{E}}^* + \vec{\vec{E}}\vec{\vec{E}}^*\right) - |\vec{\vec{E}}|^2\vec{\vec{I}}\right]\cdot\vec{n} \tag{19}$$

The net DEP force can be found using surface integration around the particle surface. This requires interpolation of the Eulerian electric field to the particle surface. However, this Lagrangian force field must be interpolated back to Eulerian coordinate in the Navier–Stokes equation. One can avoid the forward and backward interpolation steps in the numerical calculation of electric field by introducing an Eulerian form of the DEP force density in terms of the electric potential. This form is more accurate as it avoids numerical truncation errors in the interpolation steps. The Eulerian form of DEP force density is derived as follows:

$$\vec{F}_{DEP} = \nabla\cdot\frac{1}{4}\mathrm{Re}(\tilde{\varepsilon})\left[\left(\vec{\vec{E}}\vec{\vec{E}}^* + \vec{\vec{E}}\vec{\vec{E}}^*\right) - |\vec{\vec{E}}|^2\vec{\vec{I}}\right] = \frac{1}{2}\mathrm{Re}(\tilde{\varepsilon})\left[\frac{\partial\varphi_r}{\partial x_k}\left(\frac{\partial^2\varphi_r}{\partial x_l\partial x_l}\right) + \frac{\partial\varphi_i}{\partial x_k}\left(\frac{\partial^2\varphi_i}{\partial x_l\partial x_l}\right)\right]\vec{e}_k \tag{20}$$

where $\vec{e}_k$ is the unit direction, k is the coordinate, and l is the repeating coordinate direction. The direct calculation of the DEP force density in Eq. (20) instead of surface or volume integration eliminates any special treatment to capture correct physics due to rotations of the particle or to deformations due to dielectrophoretic stretching or compression on the particle surface. Bhalla et al. [14] also presented a similar model to calculate the DEP force on particle.

3. Numerical method

In this study, we present a hybrid numerical algorithm to study the underlying physics of dielectrophoresis where two interface-resolved non-body-fitted grid methods, the immersed boundary method and the immersed interface method, are coupled together. An efficient numerical algorithm is developed to solve the quasi-electrostatic form of the reduced Maxwell equation in complex variable formulation using an immersed interface method. The complex form of electric potential and field distribution are obtained by solving Eq. (1) using the immersed interface method with a fast algorithm [19,20]. The immersed boundary method, used to solve the viscous fluid flow, is simple, easy to implement and, computationally efficient. The availability of the fluid velocity field facilitates the advection of fluid marker for visualizing the flow fields as well as particle translocation under dielectrophoresis. In the following subsections, descriptions of both methods are described with implementation details.

3.1. Electric field calculation using immersed interface method

Each set of equations for φ_r and φ_i are solved by the immersed interface method (IIM) with fast algorithm. The IIM with fast algorithm takes advantage of fast Poisson solvers and can capture sharp interface conditions accurately with large jumps in dielectric properties across the interface [19]. Here we present the immersed interface method for solving Eqs. (12)–(14) for the real part, φ_r and Eqs. (15)–(17) for the imaginary part, φ_i.

Eqs. (12)–(14) can be transformed to an equivalent problem by modifying interface flux jump condition (Eq. (14b)). Let the solution of Eqs. (12)–(14) be φ_r^* and define $g(s) = [\frac{\partial\varphi_{r,f}^*}{\partial n} - \frac{\partial\varphi_{r,p}^*}{\partial n}](s)$, the jump in the normal derivative along the interface. Thus, φ_r^* satisfies Eqs. (12)–(14) with Eq. (14b) replaced by Eq. (21) [19].

$$\frac{\partial\varphi_{r,f}}{\partial n} - \frac{\partial\varphi_{r,p}}{\partial n} = g(s) \tag{21}$$

Further details of preconditioning and transformation of a general elliptic interface equation to an equivalent problem can be found in [19].

The flux jump conditions are determined through an iterative process described later with a flow chart in Fig. 2(a). In the following section, we describe the numerical solution process of the general immersed interface method for known jump conditions.

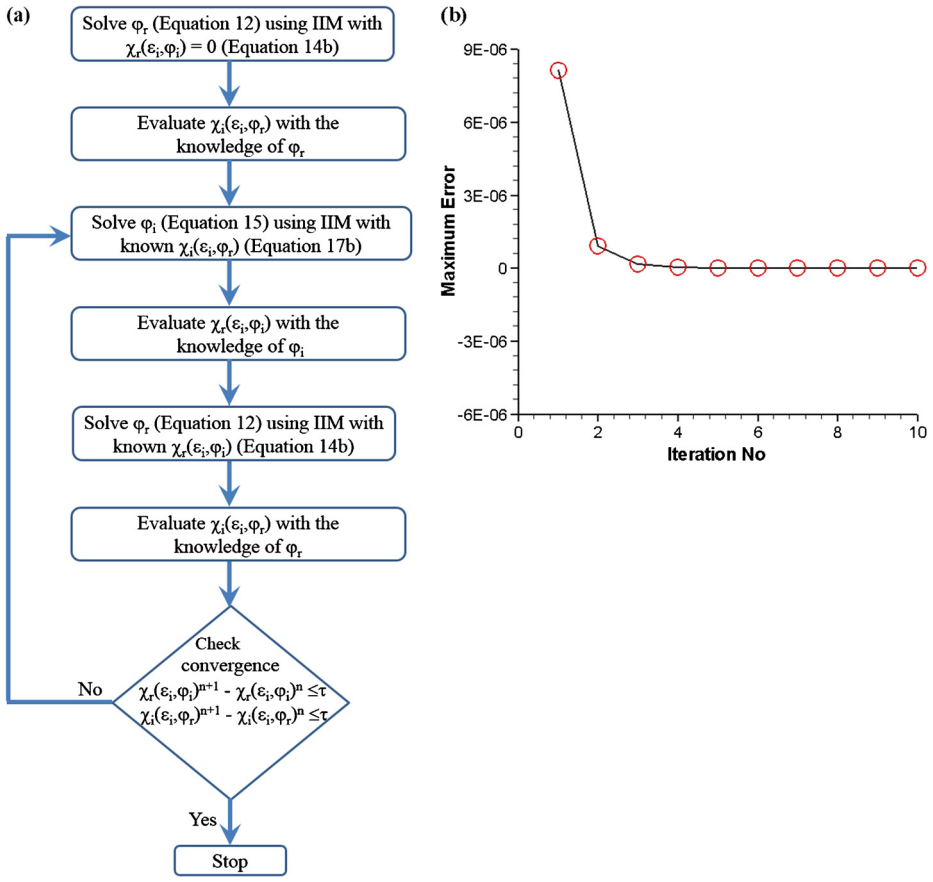

Fig. 2. (a) Flow diagram of the developed algorithm to solve complex variable quasi-electrostatic equation using immersed interface method by decoupling real and imaginary parts for efficient and faster computation. (b) Convergence of interface flux condition using our algorithm for problem shown in Fig. 1(a) with $a = b = 250$ μm. The applied AC electric potentials at the top and bottom electrodes are $\varphi_1(V_{p-p} = 10$ V; $f = 1$ MHz; $\beta = 0°)$ and $\varphi_0(V_{p-p} = 10$ V; $f = 1$ MHz; $\beta = 180°)$, and remaining boundaries were considered as insulated. A 20 μm diameter particle with $\tilde{\varepsilon}_p = 2.55\varepsilon_0 + 1.0\text{E}{-7}/(j\omega)$ is located in the middle of the fluid domain with $\tilde{\varepsilon}_m = 80\varepsilon_0 + 1.0\text{E}{-4}/(j\omega)$.

The immersed interface is represented as a cubic spline passing through a set of control points (X_k, Y_k) where $k = 1, 2, \ldots, N$. The discrete form of $g(s)$ is written as $G = [G_1, G_2, \cdots, G_N]^T$. Based on the immersed interface method and the finite difference formulation, Eqs. (12)–(14) is discretized in a uniform Cartesian grid with equal mesh size of h as

$$\frac{\varphi_r^{m+1,n} + \varphi_r^{m-1,n} - 4\varphi_r^{m,n} + \varphi_r^{m,n+1} + \varphi_r^{m,n-1}}{h^2} = C^{m,n} \quad 1 \le m \le p-1,\ 1 \le n \le q-1 \tag{22}$$

where p and q are number of grid points in x and y coordinates respectively, and m, n is the arbitrary grid point. The correction term $C^{m,n}$ is zero except at irregular grid points as shown in Fig. 1(b). Additionally this correction term can be used to estimate DEP force in Eq. (20) for better accuracy. In matrix–vector form, the discretization of Eqs. (12)–(14) can be written as

$$A\varphi_r + BG = \lambda \tag{23}$$

where A and B are two matrices and G is the discrete form of the interface jump condition $g(s)$ in Eq. (21), and λ is a vector. BG is the corresponding correction term due to the interface jump condition in Eq. (22). If G is zero, then $A\varphi_r = \lambda$ is a linear system of discrete equations without interface. G is determined such that it satisfies the flux jump condition along the interface as given in Eq. (14b). The interface condition in Eq. (21) can be written in matrix vector form as

$$U\varphi_r + QG = \gamma \tag{24}$$

where U and Q are matrices and γ is a vector. These two linear systems of equations (Eqs. (23) and (24)) are solved simultaneously in two steps. First, φ_r is eliminated to obtain a smaller system for G using matrix manipulation as

$$KG = P \tag{25}$$

where $K = (Q - UA^{-1}B)$ and $P = \gamma - UA^{-1}\lambda$. This system of G can be solved using a GMRES matrix solver if the right hand side and matrix vector product are known. These can be found by determining the residuals with an initial guess for G (for example, $G = 0$) as follows:

$$P = \gamma - UA^{-1}\lambda = \gamma - U\varphi_r(G = 0) = -\left[U\varphi_r(G = 0) - \gamma\right] = -R(G = 0) \tag{26}$$

and

$$KG = QG + U\varphi_r(G) - UA^{-1}\lambda = R(G) - R(G = 0) \tag{27}$$

With an initial guess for G, the solution of φ_r is found from Eq. (22) or (23) using a fast Poisson solver. The right hand side and matrix vector product for Eq. (25) are determined from residuals by a weighted least squares interpolation scheme. The details of the weighted least square interpolation scheme can be found in [19]. With the knowledge of G, the corrections terms are calculated and added to right hand side of the finite difference scheme (Eq. (22) or (23)) and solved for the solution φ_r. This requires successive calls to the fast Poisson or matrix solver to obtain G. In this study we used the PARDISO matrix solver from Intel Math Kernel as our Poisson solver [24,25].

The algorithm of solving φ_r using the immersed interface method can be summarized as follows:

1. Solve the systems of equation shown in (Eq. (23)) with an initial guess of $G = 0$
2. Find the right hand side vector of Eq. (25) using Eq. (26) and solution found in Step 1 using a weighted interpolation scheme
3. Find the matrix vector product in Eq. (25) using Eq. (27) and solution found in Step 1 with a weighted interpolation scheme
4. Solve Eq. (25) using GMRES matrix solver and determine G
5. Solve Eq. (23) with G found in Step 4
6. Find the matrix vector product in Eq. (25) using Eq. (27) and solution found in Steps 1 & 5, and the weighted interpolation scheme
7. Solve Eq. (23) with known G from Step 4
8. Repeat steps 4–7 until it meets the certain tolerance limit for GMRES solver to get the right G

The imaginary part of the governing equation is solved in similar way. However, both real and imaginary parts of the equations are coupled through the interface flux jump conditions as shown in Eqs. (14b) and (17b). It is necessary to have the solution of real part of the equation to determine the interface flux jump in the imaginary part of the equations and vice-versa. Therefore we developed an iterative algorithm where the real part of the equation is solved with an initial guess for the interface flux jump. Then the imaginary part of the equations are solved with immersed interface method as described above where the interface flux jump condition are determined with the knowledge of the solution of real part of the equation. This process continues until the solution provides an accurate interface flux jump condition for both equations. This iterative algorithm is described in Fig. 2(a) as a flow chart. With the knowledge of potential distribution in complex variable form, the electric field distribution can be readily obtained from Eq. (4) and the dielectrophoretic force is found using MST method as described in the previous section.

3.2. Fluid flow using immersed boundary method

The immersed boundary method is employed to study hydrodynamic effects such as motion and deformation of rigid or flexible object immersed in fluid as well as particle–fluid interactions. An Eulerian force field, $\vec{F}_{IB}$, in the fluid domain represents the contributions of forces due to the rigid and/or flexible boundaries, $\Gamma_p(t)$, of the suspended particles.

$$\vec{F}_{IB}(\vec{x}, t) = \int_{\Gamma} \vec{f}(s, t)\delta\left[\vec{x} - \vec{X}(s, t)\right]ds. \tag{28}$$

Here $\vec{X}(s, t)$ is a parameterization of $\Gamma_p(t)$, s is a Lagrangian parameter, $\vec{x} = (x, y)$ is spatial position in Eulerian variables, $\delta(\vec{x})$ is the two dimensional Dirac delta function used to establish communication between Lagrangian and Eulerian variables. The Lagrangian force $\vec{f}(s, t)$ is the elastic force that rigid and flexible particles exert in the fluid domain.

Depending on the immersed boundaries and material properties, the contribution of this force field, $\vec{f}(s, t)$ can be derived from stretching, bending or tethering of immersed boundaries. The rigidity or the flexibility of the particle boundaries under the action of hydrodynamic stretching are modeled with elastic links between immersed boundary points on the boundaries. In this study, each immersed point on a particle boundary is considered to be connected with all other immersed boundary points on the particle boundary. The stretching force contribution $\vec{f}^{qd}_{stretch}$ of an immersed boundary point $\vec{X}_q$ due to elastic links with the immersed boundary point $\vec{X}_d$ is obtained using Hook's law as follows:

$$\vec{f}^{qd}_{stretch} = S\left(\left\|\vec{X}_q - \vec{X}_d\right\| - s^{qd}_0\right)\frac{\vec{X}_q - \vec{X}_d}{\left\|\vec{X}_q - \vec{X}_d\right\|} \tag{29a}$$

where s_0^{qd} is the resting length between immersed boundary points X_q and X_d. The stretching force at $\vec{X}_d$ due to the elastic link to $\vec{X}_q$ is given by $\vec{f}_{stretch}^{dq} = -\vec{f}_{stretch}^{qd}$. The total stretching force contribution for the immersed boundary point $\vec{X}_q$ is given by $\vec{f}_{stretch}^{q} = \sum_{r=1}^{n_b} \vec{f}_{stretch}^{qd}$ where $d = 1, 2, \cdots, N_p$ and $d \neq q$. In addition to the suspended particles, we incorporate immersed boundary walls to model the channel walls of the microfluidic device. The tether forces are applied to walls to penalize the deviation from a specified fixed position. Each immersed wall point $\vec{X}_p^w$ is connected by a tether spring to a fixed point $\vec{X}^t$. The corresponding tether force is obtained from the equation

$$\vec{f}_{tether}^{wt} = S_t\left(\left\|\vec{X}^w - \vec{X}^t\right\|\right)\frac{\vec{X}^w - \vec{X}^t}{\left\|\vec{X}^w - \vec{X}^t\right\|} \tag{29b}$$

where S_t is the tether stiffness constant. The Lagrangian elastic forces are interpolated to the Eulerian grid using Eq. (28). The Dirac delta function is represented as the product of two smooth functions, $\delta(\vec{r}) = \delta_h(x)\delta_h(y)$. The Dirac delta function $\delta_h(\xi)$ with mesh width of h is given by [21]

$$\delta_h(\xi) = \begin{cases} \frac{1}{4h}[1 + \cos(\frac{\pi\xi}{2h})] & \text{if } \|\xi\| < 2h \\ 0 & \text{if } \|\xi\| \geq 2h. \end{cases} \tag{30}$$

This smoothing profile uses only a small number of grid points near the immersed boundary points. Unlike the elastic/stretch and tether forces, the dielectrophoretic force density $\vec{F}_{DEP}$ can be obtained directly in Eulerian form (Eq. (20)). The total force field due to the presence of immersed boundaries and dielectrophoresis is given by

$$\vec{F} = \vec{F}_{IB} + \vec{F}_{DEP}. \tag{31}$$

The governing Eqs. (5), (6) are discretized with the appropriate force functions described above using a finite difference scheme [21–23]. The discrete form of Eqs. (5), (6) with a regular mesh width of h is given by

$$\rho\left(\frac{\vec{u}^{n+1} - \vec{u}^n}{\Delta t} + \sum_{\lambda=x,y} \vec{u}_\lambda^n D_\lambda^{\pm}\vec{u}^n\right) = -D^0 p^{n+1} + \mu \sum_{\lambda=x,y} D_\lambda^+ D_\lambda^- \vec{u}^{n+1} + F^n \tag{32}$$

$$D^0\vec{u}^{n+1} = 0 \tag{33}$$

where λ is the coordinate direction $\lambda = x, y$, D^+ is the forward difference operator, D^- is the backward difference operator, D^0 is the central difference operator and $D^{\pm}$ is the upwind difference operator.

The discretized immersed boundary equations for fluid flow shown in Eqs. (32), (33) are solved in a method presented in [22,23,26]. In Eq. (32), a semi-implicit method is used for fluid velocities on the right hand side of the equation and the pressure p are represented at time t^{n+1}. An upwind scheme is used for nonlinear momentum and a forward difference scheme is used for the time derivative. The force field $\vec{F}$ and the fluid velocities in the nonlinear momentum term are represented at time t^n. A central difference scheme is used for the continuity equation where the fluid velocities are represented at time t^{n+1}. This transient immersed boundary fluid flow equations are solved using Fast-Fourier-Transform (FFT) methods [22,23,26]. Finally the velocity of the particle is obtained by advecting the immersed boundary at the local fluid velocity as

$$\frac{\partial}{\partial t}\vec{X}(s,t) = \vec{u}\left[\vec{X}(s,t),t\right] = \int_{\Omega} \vec{u}(\vec{x},t)\delta\left[\vec{x} - \vec{X}(s,t)\right]d\vec{x} \tag{34}$$

where, as in Eq. (28), we use a numerical integration using the discrete representation of $\vec{u}$ and the approximate interpolation function shown in Eq. (30). The numerical algorithm for viscous flow problem with IB equations can be briefly summarized as follows. With the knowledge of fluid velocities $\vec{u}^n$ and configuration of immersed particles $\vec{X}^n$ at time t^n, the fluid velocities $\vec{u}^{n+1}$ and configuration of the particles $\vec{X}^{n+1}$ are evaluated at time t^{n+1} as follows:

1. Find dielectrophoretic force densities $\vec{F}_{DEP}^n$ from potential distribution using Eq. (20).
2. Calculate elastic force densities $\vec{f}_{stretch}^n$ at each immersed boundary points with current configuration, $\vec{X}_p^n$ using Eq. (29a).
3. Calculate tether force densities $\vec{f}_{tether}^n$ at each immersed wall with current configuration, $\vec{X}_w^n$ using Eq. (29b).
4. Interpolate elastic force densities, $\vec{f}_{stretch}^n$ (Eq. (29a)) and $\vec{f}_{tether}^n$ (Eq. (29b)) into Eulerian force densities $\vec{F}_{IB}^n$ (Eq. (28)) using an approximate Dirac delta function (Eq. (30)).
5. Solve the Navier–Stokes equation with total force densities, $\vec{F}^n = \vec{F}_{DEP}^n + \vec{F}_{tether}^n + \vec{F}_{stretch}^n$, to obtain the fluid velocities $\vec{u}^{n+1}$ using Eqs. (32), (33).
6. Advect the immersed boundary points at the local fluid velocities using Eq. (34) to obtain $\vec{X}^{n+1}$.

Table 1
Grid refinement analysis of immersed interface electrostatic problem for potential distribution.

Number of grids	L^2 norm		L^∞ norm	
	Error estimation	Convergence rate	Error estimation	Convergence rate
32×16	8.46542957E−06	0.939	0.225115954	0.895
64×32	4.41402458E−06	3.41	0.121261914	3.01
128×64	4.14571387E−07	3.65	0.015397896	3.42
256×128	3.28973487E−08		0.00141513269	

4. Validation and error analysis

4.1. Convergence study

In this section, we investigate the convergence of our algorithms for obtaining the solution of complex quasi-electrostatic governing equation by solving equations for the real and imaginary parts. As mentioned earlier, the algorithm was developed to satisfy the coupled interface flux jump conditions. Fig. 2(b) shows that the interface conditions converge rapidly and obtain an accurate interface flux condition within a few iterations.

The grid refinement analysis was performed for the immersed interface and immersed boundary algorithms. The error of the electric potential solution at each grid was calculated by comparison with the finest grid solution as

$$E^N(\varphi) = \left|\varphi^N - \Pi^{N^* \to N}\varphi^{N^*}\right| \tag{35}$$

Here for simplicity we denote the complex electric potential as φ. The electric potential φ_i^N and $\varphi_i^{N^*}$ were obtained for a domain of $N \times N$ and $N^* \times N^*$ rectangular grids, respectively, where N^* represents the finest grid number and $\Pi^{N^* \to N}\varphi^{N^*}$ be the restriction of φ^{N^*} to the $N \times N$ rectangular grid. Based on the error at each grid point, L^2 and L^∞ error norms for electric potential were obtained as [27]

$$L_N^2(\varphi) = \left(\sum_{x,y \in N} \left|E^N(\varphi)\right|^2 \Delta x \Delta y\right)^{\frac{1}{2}} \tag{36}$$

and

$$L_N^\infty(\varphi) = \max_{x,y \in N}\left|E^N(\varphi)\right| \tag{37}$$

where N is the uniform grid with mesh width of $\Delta x, \Delta y$, where $\Delta x = \Delta y$. The rate of convergence in L^2 and L^∞ norms are obtained as

$$K_2^N(\varphi) = \log_2\left(\frac{L_N^2(\varphi)}{L_{N^*}^2(\varphi)}\right) \tag{38}$$

$$K_\infty^N(\varphi) = \log_2\left(\frac{L_N^\infty(\varphi)}{L_{N^*}^\infty(\varphi)}\right) \tag{39}$$

For the convergence study of IIM, we placed a single 50 μm in diameter particle at the center of 500 μm × 250 μm rectangular domain. A peak to peak potential difference of 10 V was prescribed between top and bottom boundaries. The left and right boundaries were insulated. In all studies the fluid was assumed to be water with conductivity $\sigma_f = 1.0\text{E}{-4}$ S/m, permittivity $\varepsilon_f = 80\varepsilon_0$ with free space permittivity $\varepsilon_0 = 8.85\text{E}{-12}$ Fm^{-1}. The conductivity of the particle was assumed to be 1.0E−7 S/m and permittivity $\varepsilon_f = 2.5\varepsilon_0$. The error analysis and the order of convergence for different grid sizes are shown in Table 1. The finest 512×256 grid results for potential distribution was taken as a base result to estimate errors and convergence rates for grids of 256×128, 128×64, 64×32 and 32×16. The results show that the convergence rates in the L^2 and L^∞ norms are second order except on the coarsest grid of 32×16. The convergence rate is poor on the grid of 32×16 because there is insufficient resolution on the coarsest grid for a fixed cell diameter.

For convergence rate of fluid velocities $\vec{u}$, error norms are defined in a similar way. However, as the fluid flow is a function of time, the order of convergence is obtained as a function of time as well. We consider a rectangular 200 μm × 100 μm domain, where a particle of 10 μm diameter is located at the middle of the domain. Two immersed wall are placed 25 μm offset from top and bottom of the computational boundary to mimic channel flow with no-slip boundary conditions on the wall. The density and viscosity of the fluid are 1000 kg/m^3 and 0.001 kg/m s, respectively and the particle is moving in horizontal direction with a pulling force of 0.005 N/m on the particle. The error estimation and rate of convergence in the L^2 and L^∞ norms are calculated over a period of 0.4 s. Table 2a and Table 2b show error analysis for L^2 and L^∞ norms, respectively. These results are consistent with first order convergence as expected in immersed boundary methods [28–30].

Table 2a
Grid refinement analysis of immersed boundary method.

Number of grids	L^2 norm			
	Error estimation		Convergence rate	
	u_x	u_y	u_x	u_y
64×32	6.556318E−10	6.28596E−11	0.80982673	0.811588887
128×64	3.740054E−10	3.581451E−11	1.037870328	1.168857711
256×128	1.821578E−10	1.592934E−11		

Table 2b
Grid refinement analysis of immersed boundary method.

Number of grids	L^∞ norm			
	Error estimation		Convergence rate	
	u_x	u_y	u_x	u_y
64×32	9.099821E−06	1.868527E−06	0.9299136	0.942369968
128×64	4.776403E−06	9.723391E−07	1.103573681	1.006903999
256×128	2.222758E−06	4.838485E−07		

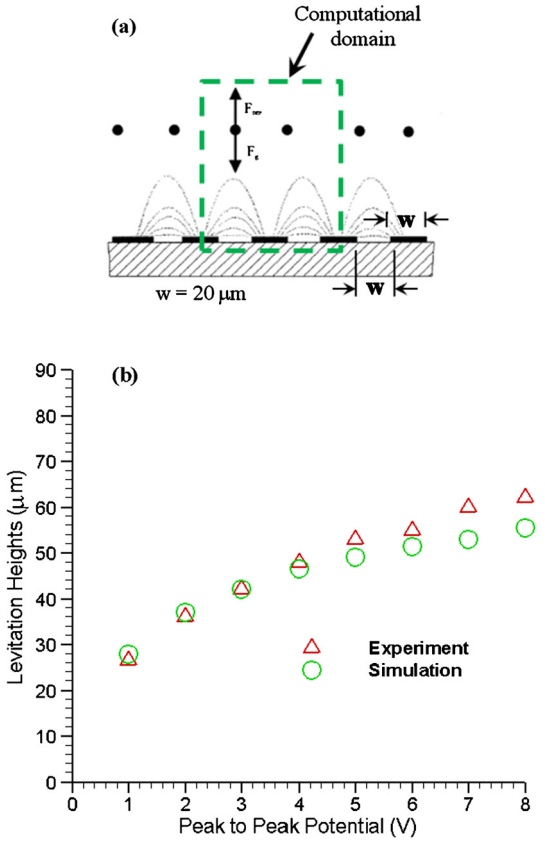

Fig. 3. (a) The computational domain used to compare our numerical results with the experimental results reported in Markx et al. [28]. (b) Comparison of levitation heights predicted by numerical model and experimental observations [28]. The AC electric field frequency is 1 MHz.

4.2. Model validation

In order to validate our hybrid numerical model for dielectrophoretic particle transport, we present a comparison between our numerical results and previously published experimental results of Markx et al. [28] where the dielectrophoretic levitation heights of latex beads were measured as a function of the applied potential at the electrodes. Markx et al. [28] used interdigitated microelectrodes on a bottom of a microchamber (Fig. 3(a)) to study the effect of frequency, electrode widths and applied potential on dielectrophoretic levitation of 6 microns latex beads. The width and spacing between the microelectrodes are 20 μm and the length of electrode is 1 cm. Since electrodes form parallel bars in their setup, there is

no variation of electric field along the length of electrodes (in z direction) which makes this study appropriate to compare with our two dimensional hybrid numerical model. In our numerical simulation we used an 80 μm × 80 μm computational domain with 20 μm electrode width and spacing between electrodes as shown in Fig. 3(a). The conductivity and permittivity of the buffer suspension for both the simulation and experiment were $\sigma_f = 1.1$ mS/m and $\varepsilon = 79\varepsilon_0$, and the frequency of applied potential was 1 MHz. The conductivity and permittivity of latex beads were reported in Markx et al. [28] as 4.33E−7 S/m and $\varepsilon = 2.55\varepsilon_0$, respectively and these values were used in the simulation of particle levitation without any modification.

The comparison between the numerical and experimental results of particle levitation is shown in Fig. 3(b). Our model predicts levitation heights very well at the lower range of applied potential, but underestimates the levitation height at higher applied potential. Excluding experimental uncertainty, we hypothesize that this deviation could be attributed to exclusion of thermal effects in our model. At higher electric field the temperature of the buffer increases due to the effect of joule heating [29] and the viscosity of the buffer decreases. Reduction in the viscosity provides lesser viscous drag force on the latex beads for same dielectrophoretic levitation force. The inclusion of thermal effects in the model might provide better agreement and this will be part of our future work.

4.3. DEP force with PD and MST methods

We provide a comparative study between PD and MST methods for calculating the DEP force. Here we consider a 100 μm × 50 μm domain with two electrodes on top and bottom surfaces. The fluid media is assumed to be water and the particle is immersed in the domain as shown in Fig. 1(a). The length of the top electrode was 7.8125 μm, while the bottom electrode extends across the length of the domain. The applied AC electric potentials at the top and bottom electrodes are $\varphi_1(V_{p-p} = 2\text{ V}; f = 1\text{ MHz}; \beta = 0^\circ)$ and $\varphi_0(V_{p-p} = 2\text{ V}; f = 1\text{ MHz}; \beta = 180^\circ)$, and remaining boundaries were considered as insulated. The electrical conductivity and permittivity of the particle were 1.0E−7 S m^{-1} and $2.5\varepsilon_0$ respectively, and particle radius was varied to analyze the effect of particle size. The potential and electric field distributions were evaluated with and without particle to calculate DEP force using MST and PD methods, respectively. The DEP force based on PD method is given by

$$\vec{F}_{DEP} = 4\pi r^3 \varepsilon_f \,\text{Re}(\tilde{\chi})\vec{E}_{rms} \cdot \nabla \vec{E}_{rms} \tag{40}$$

where r is the radius, ε_f is the permittivity and $\tilde{\chi}$ is the complex Clausius–Mossotti factor. Two different particle positions were considered: (i) the particle was far away from the top electrode and (ii) the particle was near the top electrode. Calculated DEP force from both approaches is similar when the particle is small and the particle's position is far away from the top electrode as shown in Figs. 4(a)–(b). Differences between DEP forces are noticeable for 3 μm radius particle. The differences increase as the particle radius increases. When the particle is small compared to the electrode and domain size and far away from the energized electrode, the overall nature of the electric field remains uniform. This is due to the fact that when particles are small the deformation of electric potential lines due to the particle is negligible. Therefore the two approaches produce similar results. In the second case when the particle is near the top electrode, the discrepancy between two approaches is more pronounced even for small particles as shown in Figs. 4(c)–(d). Particles near top electrode alter the potential distribution and electric field significantly as we will show later in Fig. 5. In both cases, the difference in the x component of DEP force increases significantly with increasing particle size (see Fig. 4(a, c)). The difference in the y component of DEP force is even greater in the latter case (see Fig. 4(d)). We assert that the MST method calculates the DEP force more accurately since no approximations are used. The discrepancy between the two methods cannot be entirely eliminated by using higher order multipolar terms such as quadrupole or octapole since in the EDM approach the electric field is computed without considering the physical effect of the particle on the electric field.

5. Results and discussion

5.1. Study of AC dielectrophoresis with single particle

To study the physics of AC dielectrophoresis, we consider a particle of 7.5 μm diameter suspended in a fluid as shown in Fig. 5(a). The electrode configurations in this kind of setup provides a highly nonuniform electric field distribution which is essential to facilitate dielectrophoresis. Similar electrode configuration has been used in reported experimental demonstration [30]. The applied AC electric potentials at different electrodes are $\varphi_1 = \varphi_2 = \varphi_3(V_{p-p} = 1\text{ V}; f = 1\text{ MHz}; \beta = 0^\circ)$ and $\varphi_4(V_{p-p} = 1\text{ V}; f = 1\text{ MHz}; \beta = 180^\circ)$. The potential distribution, electric field and DEP force were evaluated by placing the particle at $c_x = 75$ μm and $c_y = 63$ μm. The dielectric constant and conductivity of particle were taken as $2.5\varepsilon_0$ and 1.0E−7 S/m which corresponds to typical biological cell membrane properties. Water was considered as the fluid media with dielectric properties as mentioned in previous section. The potential distribution, electric field vectors and DEP force vectors are shown in Fig. 5(b)–5(d). Fig. 5(b) shows that the potential distribution is deformed by the presence of the particle. There is a sharp potential drop within the particle since the conductivity and permittivity of the particle is much less than that of the fluid media. In Fig. 5(c), the electric field vectors are deflected away from the particle surface. The lower electric field regions are found on the top and bottom sides of the particle and the higher electric field region is found on

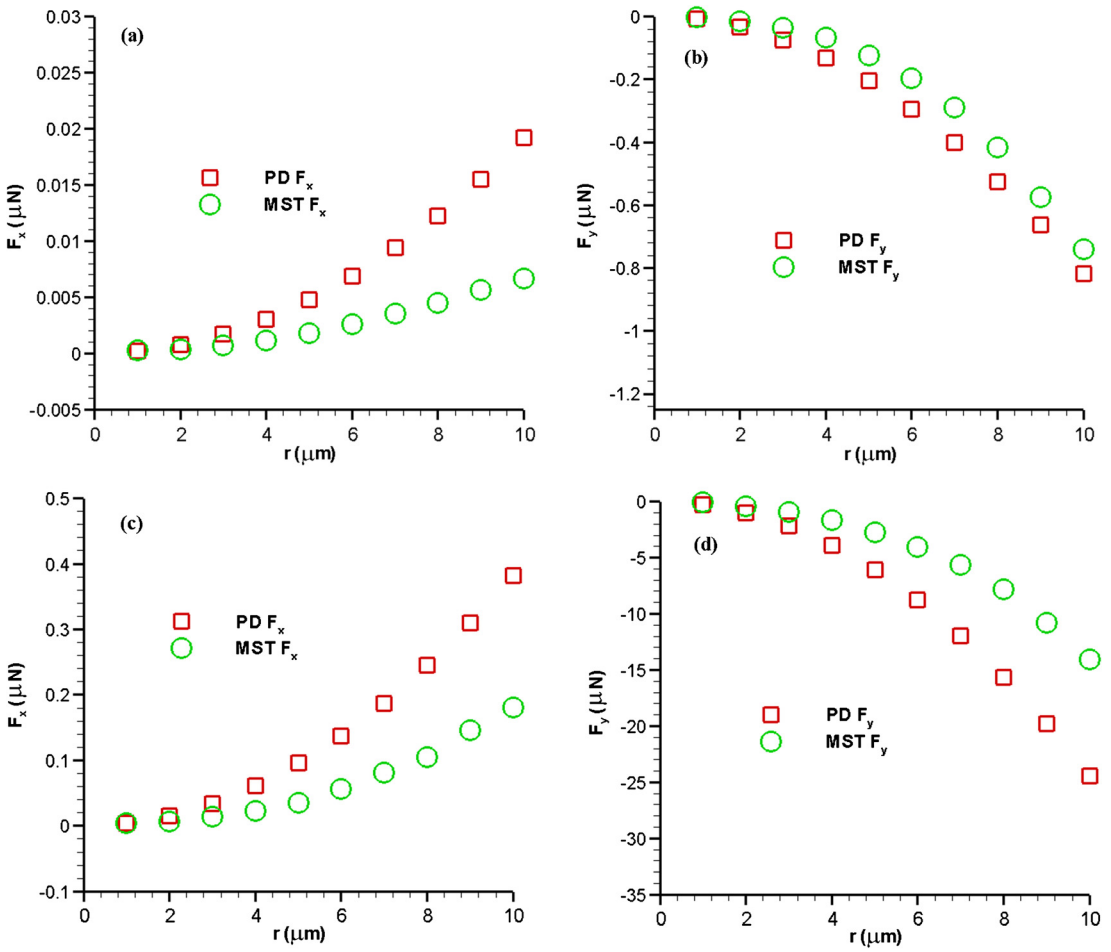

Fig. 4. DEP forces in (a) x and (b) y direction for particle's center position at $x = 50$ μm and $y = 12.5$ μm based on Maxwell stress tensor (MST) and point dipole (PD) methods. Significant deviation between the two methods is seen at particle radius of 3 μm and higher. DEP forces in (c) x and (d) y direction for particle's center position at $x = 50$ μm and $y = 37.5$ μm based on MST and PD methods. Deviation between two methods is more pronounced when particle is closed to the top electrode.

the left and right sides of the particle. Since the particle is less polarizable than the fluid media, an accumulation of charge develops at the interface opposing the electric field. In this scenario, the particle is working as an insulator compared to fluid media. Hence the electric field outside the particle is tangential to the particle surface.

Fig. 5(d) shows the DEP force vectors obtained based on the Maxwell stress tensor. The Eulerian distribution of DEP force is computed using Eq. (20). The net force is directed downwards to the lower electric field region indicating that the particle experiences negative dielectrophoresis. As the dielectric constant and electrical conductivity of the particle is lower than that of the fluid media, the mode of dielectrophoresis cannot be changed from negative to positive by changing applied frequency alone. This explains the reason for having negative dielectrophoresis in most biological cell manipulation experiments [31]. *It is interesting to note that negative DEP force is compressive in nature to the particle surface, while positive DEP force is tensile in nature (not shown here). The compressive or tensile DEP force is important in biological cell manipulation since it has great impact on cell proliferation and differentiation. For example, in regenerating tissue from mesenchymal into bone, cartilage, or fibrous tissue, compressive stress stimulates chondrogenesis, while high tensile strain stimulates the net production of fibrous tissue* [32].

Dielectrophoretic motion of a single particle with full hydrodynamics is presented for various initial particle locations. The fluid media was considered as stationary i.e. there is no background flow within the domain. We set the particle's initial location at an elevation of $c_y = 63$ μm with three different horizontal locations: a) $c_x = 53$ μm, b) $c_x = 75$ μm, and c) $c_x = 97$ μm. As the spatial variation in the electric field depends on particle location, particles experience different degrees of DEP force and hence the particle trajectories vary. The dielectrophoretic particle translocations are shown in Figs. 6(a)–6(c). In all cases, the particles experience negative dielectrophoresis as the particle is less polarisable than the media. Under negative dielectrophoresis, particles move away from the top electrode toward the bottom electrode where the intensity of electric field is the lower. The particle located at the center moves straight downward and the particle located offset from the center moves away from the nearest edge of the top electrode. The particle trajectory in negative dielectrophoresis indicates that at early time steps the particles move faster and at later time steps the particle speed is

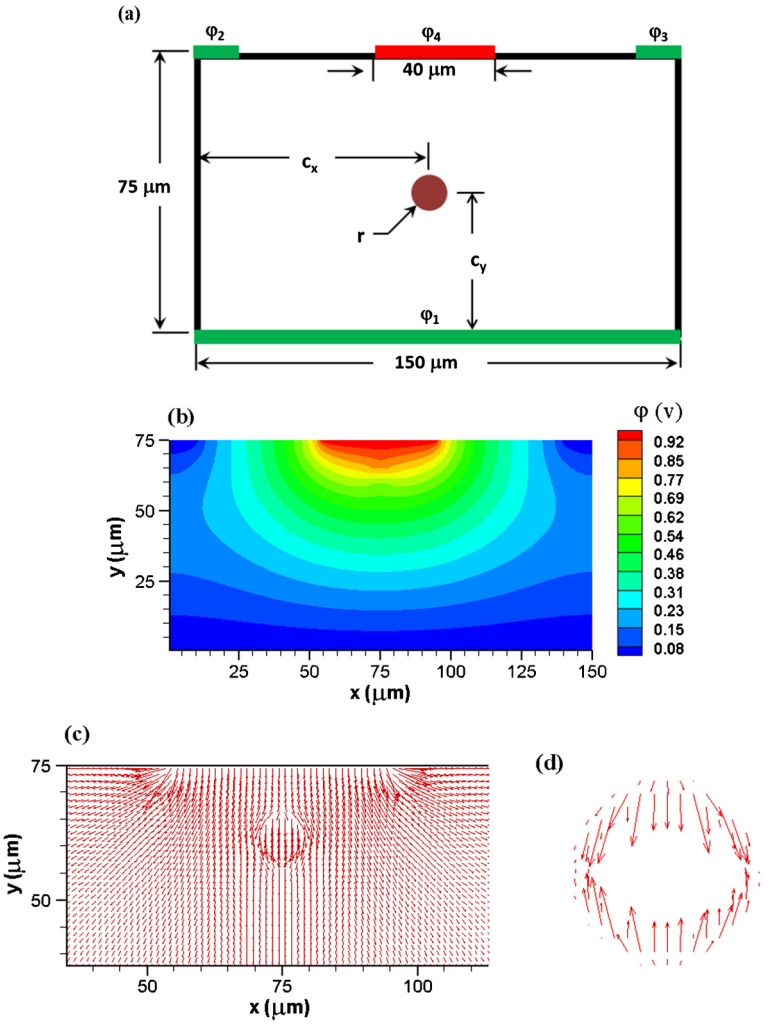

Fig. 5. (a) Schematic of a single particle dielectrophoresis setup. (b) Contour plot for potential distribution. (c) A close view of electric field vectors around the particles, (d) DEP force vector due to the applied electric field. Here $c_x = 75$ μm, $c_y = 63$ μm and $r = 3.75$ μm, and the applied AC electric potentials at different electrodes are $\varphi_1 = \varphi_2 = \varphi_3 (V_{p-p} = 1$ V; $f = 1$ MHz; $\beta = 0°)$ and $\varphi_4 (V_{p-p} = 1$ V; $f = 1$ MHz; $\beta = 180°)$. The dielectric properties of particles and fluid are $\tilde{\varepsilon}_p = 2.5\varepsilon_0 + 1.0\text{E}{-7}/(j2\pi f)$ and $\tilde{\varepsilon}_p = 80\varepsilon_0 + 1.0\text{E}{-4}/(j2\pi f)$, respectively.

significantly slower. This is due to the weakening of the repulsive DEP force as the particle moves away from the higher electric field gradient region. The streamlines for the fluid flow due to the particle motion are shown in Fig. 6(d) for case *b* ($c_x = 75$ μm). The anti-clockwise vortices on the two sides indicate that the particle is moving away from the higher electric field region at the top.

5.2. Dielectrophoretic particle trap

In this section, we used the hybrid numerical method to study dielectrophoretic particle trapping. The design of the particle trap is shown in Fig. 7(a) where two microchannels intersect and create a trapping zone at the intersection with application of appropriate AC potential at two pairs of electrodes. A 7.5 μm diameter particle was employed for the particle trapping study. The particle was initially located within the left channel and was 40 μm away from the center of microchannel junction. All conditions and properties of the particle remain the same as in Section 5.1 and DI water was considered as the buffer. The applied electric potentials at the horizontal and vertical electrodes are $\varphi_1 = \varphi_2 (V_{p-p} = 3.5$ V; $f = 1$ MHz; $\beta = 0°)$ and $\varphi_3 = \varphi_4 (V_{p-p} = 3.5$ V; $f = 1$ MHz; $\beta = 180°)$. The electric field distribution (Fig. 7(b)) shows that the lowest electric field intensity can be found at the center of the intersection. Here the particle undergoes negative dielectrophoresis due to its lower polarizability compared to the buffer. Thus, a negative DEP force drives the particle towards the center of the junction because of the lower electric field intensity. The movement of the particle induces flow in the fluid which is shown in Fig. 7(c) as flow streamlines. The particle pushes the adjacent fluid in vertical direction as it moves in the horizontal direction. At the junction, fluid can move upward and downward direction without much resistance due to the wide verti-

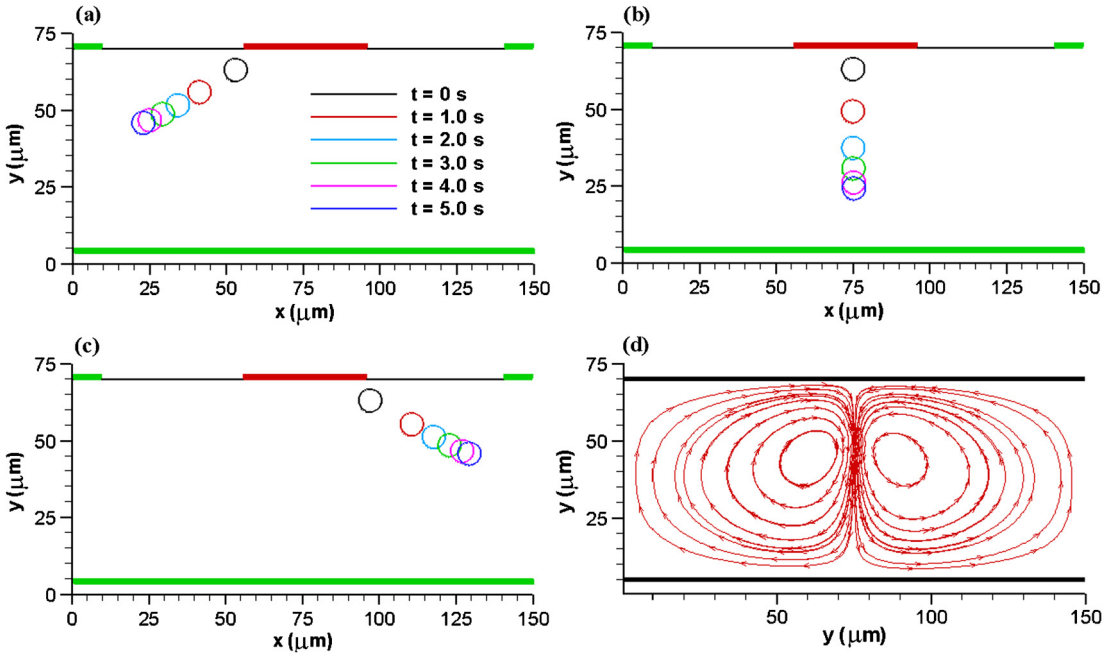

Fig. 6. Particle trajectories for various initial positions of a particle in negative dielectrophoresis. The computational domain, applied electric potential, and properties of particle and fluid media were the same as provided in Fig. 5. The particle moves away from the higher electric field region near the top electrode from its initial elevation of $c_y = 63$ μm. The initial x-locations of the particle are (a) $c_x = 53$ μm, (b) $c_x = 75$ μm, and (c) $c_x = 97$ μm. (d) Flow streamlines at 1 s for initial particle location of $c_x = 75$ μm and $c_y = 63$ μm.

cal channel opening as observed in the streamline profiles shown in Fig. 7(c). It is interesting to note that fluid circulates around the junction as there was no external pressure gradient in the system.

Particle positions as a function of time are shown in Fig. 7(d). In the initial stage, the particle moves slowly, but it accelerates as it moves closer to the trapping point where the DEP force drops to zero. From the electric field contour diagram it is evident that the degree of spatial nonuniformity in the electric field is greater within a certain region of the trapping zone. Far away from the zone, the degree of nonuniformity is not as pronounced. When the particle is very close to the trapping point, the velocity of the particle decreases because the degree of nonuniformity is reduced. The particle completely stalls at the middle of the junction where the electric field is the minimum.

Fig. 8 illustrates trapping of multiple particles in the device shown in Fig. 7(a). In this case, four particles were placed at four different sites/branches. Each particle is 40 μm away from the center of the junction. Fig. 8(a) shows the electric field contours which clearly demonstrate the deformation of electric fields due to the presence of particle in the computational domain. This deformation becomes pronounced near the trapping zone where the electric field gradient is high. Fig. 8(a) also illustrates that the spatial nonuniformity in the electric field was concentrated near the center of the junction. Far away from that zone, the degree of nonuniformity is much less. The DEP forces at the boundaries of the particle are presented in Fig. 8(b). Due to negative dielectrophoresis, all particles undergo compressive force. This compressive force vector is especially relevant for trapping biological cells as they are much fragile. *It is important to note that the typical boundary integration method for calculating DEP force cannot provide the detail spatial information about the physical state of a cell during dielectrophoresis.* As spatial nonuniformities in the electric field are less pronounced far away from the trapping zone, the magnitude of the DEP force is small. However near the center of the junction, where the electric field value is low, the net DEP force is high. This zone can be termed as the sensing zone. When particles approach the sensing zone particles move faster as shown in Fig. 8(c) and then decelerate as they come close to the point of global electric field minima. Near the minimum gradient of electric field, particle speeds approach zero. Multiple particles trapping takes longer time compared to the single particle trapping. This may be due to greater hydrodynamic resistance as well as mutual interactions between particles. As the four particles move toward the junction they induce flow opposite to each other. The opposite flow provides greater hydrodynamic drag. It is interesting to note that no particle can reach to the center of the junction. However in longer simulation we observed that the particles begin to rotate around the point of electric field minimum. In a longer simulation we observed that one particle was able to reach to the center of junction, the electric field minimum, by breaking symmetry of the particle cluster. We are not sure if this symmetry breaking is due to numerical artifacts or some other means. We along with our experimental collaborators plan to study this experimentally to verify this numerical observation.

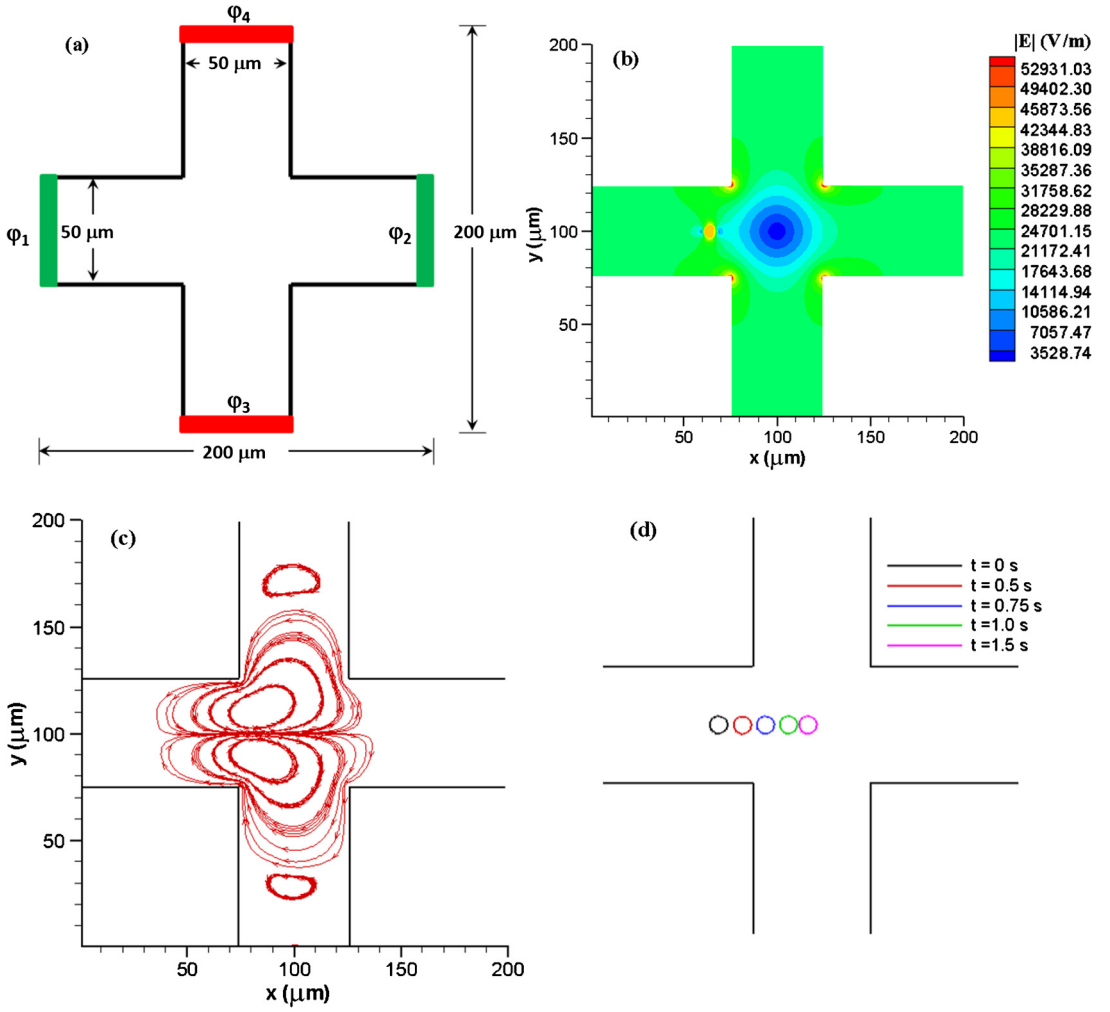

Fig. 7. (a) Schematic of a dielectrophoretic trap using a cross-channel configuration. The channel is filled with water and a particle is initially located on the left branch (60 μm, 100 μm) of the cross-channel. (b) Electric field contour diagram. The lowest electric field is found at the center of junction for stable trapping of particles. (c) Fluid flow streamlines induced by dielectrophoretic motion of particle at 0.5 seconds for an initial particle location shown in figure a. (d) Trajectory of particle as a function of time. Here the applied electric potentials at the horizontal and vertical electrodes are $\varphi_1 = \varphi_2 (V_{p-p} = 3.5\ \text{V};\ f = 1\ \text{MHz};\ \beta = 0^\circ)$ and $\varphi_3 = \varphi_4 (V_{p-p} = 3.5\ \text{V};\ f = 1\ \text{MHz};\ \beta = 180^\circ)$.

5.3. Dielectrophoretic particle assembly

The application of dielectrophoresis has been reported in the literature for biological cell aggregation to facilitate tissue generation, stem cell research, etc. In this section we will demonstrate the physics of bioparticle assembly under dielectrophoresis using the hybrid numerical method. Fig. 9(a) illustrates a computational domain (150 μm × 150 μm) filled with water and randomly orientated bioparticles. The diameter of each particle is 11.25 μm, and dielectric constant and electrical conductivity of each particle are 2.5 and 1.0E−7 S/m to resemble typical cell membrane electrical properties. The applied electric potentials at the left and right electrodes are $\varphi_1 (V_{p-p} = 1.5\ \text{V};\ f = 1\ \text{MHz};\ \beta = 0^\circ)$ and $\varphi_2 (V_{p-p} = 1.5\ \text{V};\ f = 1\ \text{MHz};\ \beta = 180^\circ)$, respectively.

Fig. 9(b) shows the normalized combined electric field contours and electric field lines with embedded particles. Although the applied potentials were uniform, local distortions of the electric field were found due to the presence of particles of different dielectric properties in the suspending media. This local nonuniformity in the electric field causes dielectrophoresis and hence assembly of particles. It is noteworthy to mention that dielectrophoretic force calculations based on the point dipole moment method cannot predict this kind of dielectrophoresis as it does not consider the nonuniformity of electric field due to the presence of particle. Fig. 9(b) shows that the electric field lines are deflected away from the particle surface and the particles behave like insulators.

Transient multiple particle interactions and assembly are shown in Fig. 9(c) for the initial configuration as described in Fig. 9(a). The particles experience negative dielectrophoresis as they are less polarizable than the media. Due to negative dielectrophoresis, particles move towards the lower electric field region adjacent to the neighboring particles' interface. Par-

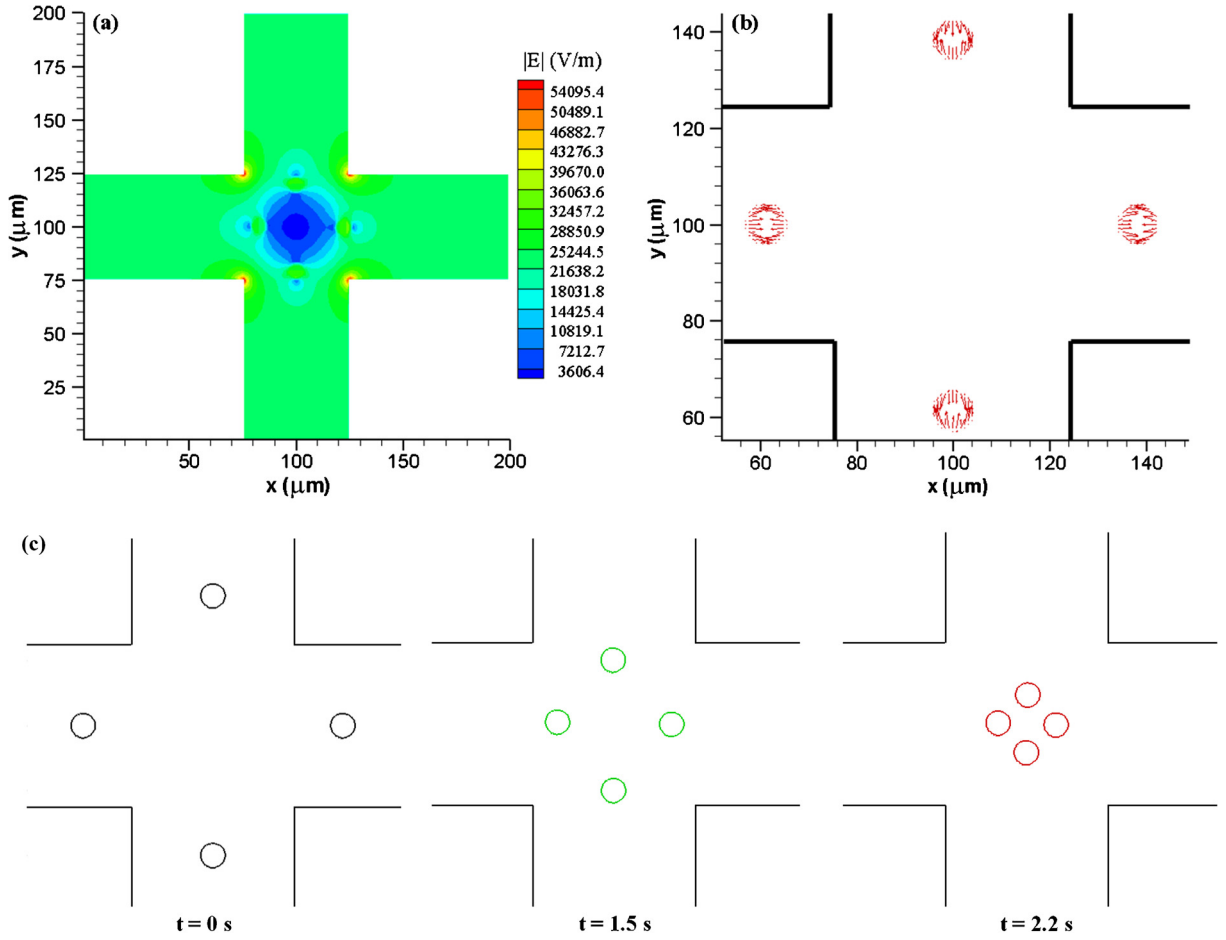

Fig. 8. (a) Electric field contour diagram with four embedded particles of diameter 7.5 μm. Initially one particle is located in each branch, and the initial distance of each particle from the centerline point of the channel was 40 μm. The dielectric properties of fluid and particles as well as the applied electric potentials are the same as in Fig. 7. (b) The dielectrophoretic force vectors acting on the boundaries of the particle. (c) Dielectrophoretic particle transport as a function of time towards the trapping zone.

ticles undergo a complex interaction because of presence of multiple particles. The simulation results indicate that particles experience both translational and rotational motion with respect to each other. In case of rotational motion, particles rotate clockwise in one situation and counter clockwise in the other to obtain the shortest path for parallel alignment with the electric field. During rotational movement, particles exhibit repulsive DEP interaction forces to facilitate the alignment and then move toward each other by attractive DEP interaction force as shown in Fig. 9(c). Once the particles align themselves they move faster toward each other; but when they are very close at a later time the attractive motion becomes retarded. This is because as the particles become closer to each other, the degree of nonuniformity in the electric field between two neighboring particle interfaces is lessened. Hence the DEP force also drops and the hydrodynamic drag force dominates over the DEP interaction force. Finally the particle velocities approach zero as they become near to each other and form a stable chain after contact.

Fig. 9(d) shows particle assembly for a different initial configuration where particles were orientated in a 30° inclined line. The mechanism of this assembly are also negative dielectrophoresis and particles move towards each others' lower electric field zone adjacent to their interface as explained above. Based on the analysis above, it can be said that DEP particle–particle interaction always leads to the chaining of particles and alignment to the electric field regardless of initial particle orientation (except unstable orientations) [33]. Also particle rotation or translation speed depends on the degree of nonuniformity in the electric field. Particle–particle interactions [34,35], assembly of different types of particles and related factors affecting the assembly mechanism has also been reported in earlier literatures [12,13,33].

6. Conclusions

A hybrid immersed interface–immersed boundary method with an algorithm for decoupling the complex version of the electrostatic equation has been presented to investigate the fundamental mechanism of AC dielectrophoresis. In this hybrid

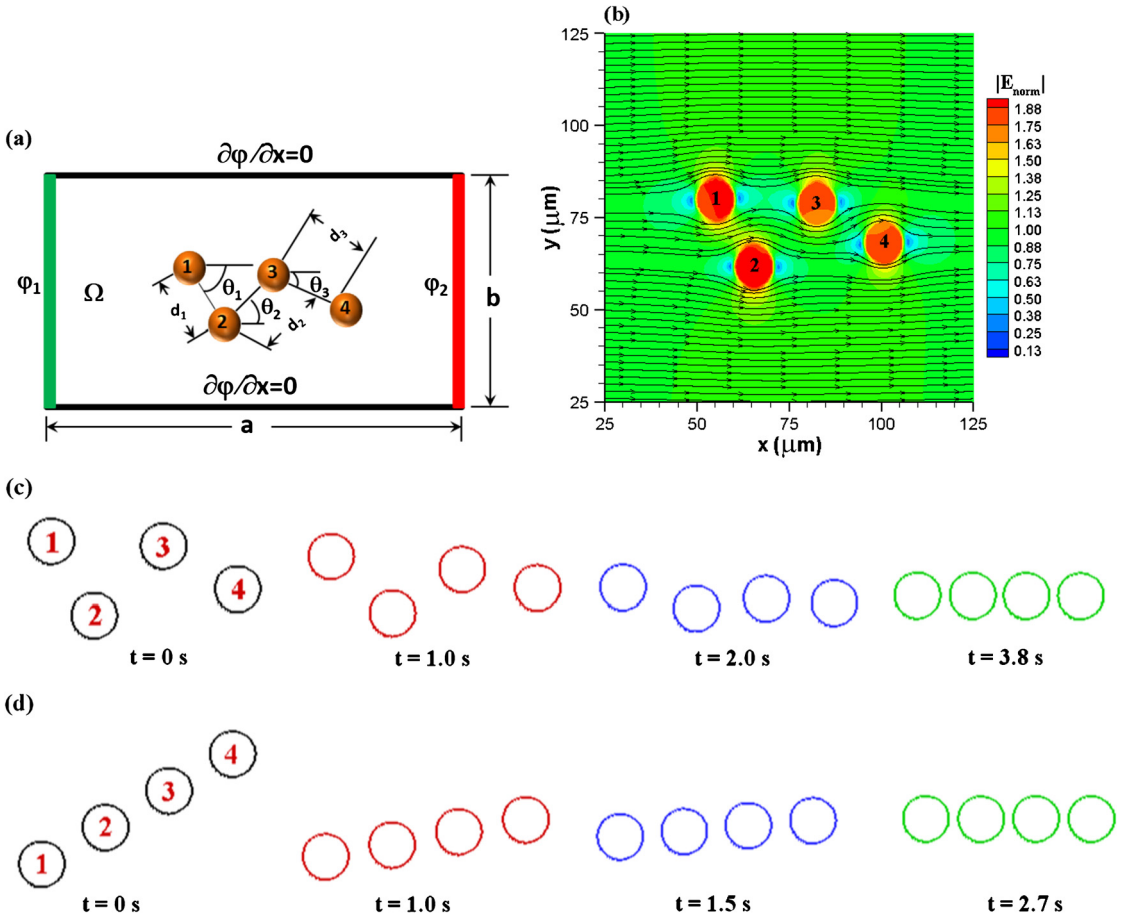

Fig. 9. (a) Schematic of computational domain for dielectrophoretic particle assembly with applied in phase and out of phase electric potential in left and right electrode, respectively. (b) Normalized electric field contour and electric field lines in media with embedded similar ($\varepsilon = 2.5\epsilon_0$ and $\sigma_p = 1.0\text{E}{-}7$ S/m) particles of 11.25 μm diameter. Here the initial configuration parameters are $d_1 = d_2 = 21$ μm, $d_3 = 24$ μm, $\theta_1 = 60°$, $\theta_2 = 45°$ and $\theta_3 = 30°$. (c) Transient particle assembly process for initial configuration as mentioned in (b). (d) Transient particle assembly process for initial orientation of $d_1 = d_2 = d_3 = 19$ μm, $\theta_1 = \theta_3 = -30°$ and $\theta_2 = 30°$. Here the applied electric potentials at the left and right electrodes are $\varphi_1(V_{p-p} = 1.5$ V; $f = 1$ MHz; $\beta = 0°)$ and $\varphi_2(V_{p-p} = 1.5$ V; $f = 1$ MHz; $\beta = 180°)$.

method, fluid flow has been solved with the immersed boundary method and complex electric potential has been solved by immersed interface method to accommodate the best features of both methods. The main feature of this hybrid method is to capture the relevant physics (viscous flow, elastic deformation, electrophysics etc.) of AC dielectrophoresis with rigid or flexible boundaries using an interface-resolved method instead of the point-particle model without dealing with the complex variables in computations. Complex variable formulations take larger memory space. The developed algorithm for solving complex differential equations converges rapidly and takes only a few iterations.

The hybrid method was first applied to a model problem of AC dielectrophoresis with one particle emerged in water. A detailed convergence analysis for both immersed interface and immersed boundary methods has also been presented. The convergence study suggests that the electric potential field convergence is second order and the convergence for the velocity field is first order. The method was validated with an experimental study of AC dielectrophoretic particle levitation. The validation results show that the numerical predictions of particle levitation are in good agreement with the experimental results.

We presented a detailed analysis of calculating dielectrophoretic force using both point dipole and Maxwell stress tensor methods. Our numerical results suggest that the point dipole method should be avoided in the case of large particles or if particles are near an energized electrode which is the case for many biological microfluidic applications. The inclusion of higher order terms in point dipole method cannot eliminate the limitations as the method does not consider the electric field variation due to the presence of particles. This comparative study provides a useful physical insight to select the appropriate method to calculate dielectrophoretic force based on the application, electrode, and domain size.

We also studied dielectrophoretic trapping of multiple particles in a cross-channel junction. The design shows that global minimum of the electric field can be created in the middle of a microchannel junction, and particles move towards the

center of the junction and get trapped under applied electric field. The acceleration and deceleration of particle velocities were observed during different phases of particle movement and an explanation behind those observations was presented.

Finally we demonstrated that this hybrid method can be applied to understand the physics behind AC dielectrophoretic multiple particle interaction and assembly for initial random orientation of particles. Our numerical results suggest that within a close proximity, particles form a chain regardless of initial orientation and locations. The local nonuniformity in the electric field due to the presence of particles facilitates this DEP assembly. Point dipole methods cannot explain this phenomena as it cannot provide the spatial nonuniformity in the electric field due to the presence of particles. It is possible to form the particle assembly, even though particles are not in close proximity. In that case, proper electrode/channel design is needed to bring particles in close proximity so that particle–particle interaction can be used for assembly.

Appendix A. Governing equation for AC electric potential

In dielectrophoresis analysis, the electric field can be obtained from quasi-electrostatic model since the time scale of particle motion is much larger than that of electric field. Ignoring magnetic field, the Maxwell equations are given by

$$\nabla \cdot \vec{D} = \rho_b \tag{A.1}$$

$$\nabla \times \vec{H} = \vec{J} + \frac{\partial \vec{D}}{\partial t} \tag{A.2}$$

where $\vec{D}$ is the electric displacement vector; $\vec{J}$, the current density; $\vec{H}$, the magnetic field vector; and ρ_b, the charge density. Taking divergence of (A.2) and substituting (A.1) we obtain the charge conservation equation

$$\frac{\partial \rho_b}{\partial t} + \nabla \cdot \vec{J} = 0 \tag{A.3}$$

For a homogeneous linear dielectric material

$$\vec{D} = \varepsilon \vec{E} \tag{A.4}$$

$$\vec{J} = \sigma \vec{E} \tag{A.5}$$

where $\vec{E}$ is the electric field; ε, the permittivity; and σ, the electrical conductivity. The AC electric potential with a frequency of ω can be written as

$$\tilde{\varphi}(\vec{x}) = \varphi(\vec{x}) e^{j\omega t} \tag{A.6}$$

where φ is the amplitude of the AC field. Substituting (A.4) and (A.6) into (A.1), we obtain the charge density

$$\rho_b = \nabla \cdot (\varepsilon \tilde{E}) = -\nabla \cdot (\varepsilon \nabla \tilde{\varphi}) \tag{A.7}$$

Taking time derivative of (A.7) and substituting (A.6)

$$\frac{\partial \rho_b}{\partial t} = -j\omega \nabla \cdot (\varepsilon \nabla \tilde{\varphi}) \tag{A.8}$$

From (A.7) with $\tilde{E} = -\nabla \cdot \tilde{\varphi}$, we get

$$\frac{\partial \rho_b}{\partial t} = j\omega \rho_b \tag{A.9}$$

Substituting in (A.9) and (A.5) in (A.3)

$$j\omega \rho_b + \nabla \cdot (\sigma \vec{\tilde{E}}) = 0 \tag{A.10}$$

Or equivalently

$$j\omega \nabla \cdot (\varepsilon \vec{\tilde{E}}) + \nabla \cdot (\sigma \vec{\tilde{E}}) = 0 \tag{A.11}$$

Taking divergence of (A.11) and dividing by $j\omega$, we obtain

$$\nabla \cdot (\tilde{\varepsilon} \nabla \tilde{\varphi}) = 0 \tag{A.12}$$

with $\tilde{\varepsilon} = \varepsilon - j\frac{\sigma}{\omega}$. This equation is the same as that used by Liu et al. [9], but differs from Bhalla et al. [14] where a current source term is introduced in the right hand side. The inclusion of current source term is not necessary for analyzing DEP problems. However, the inclusion of current source term in the governing equation makes it more general and expands the applicability of the equations for modeling other mechanism such as electrolocation [14].

References

[1] H. Morgan, A.G. Izquierdo, D. Bakewell, N.G. Green, A. Ramos, The dielectrophoretic and travelling wave forces generated by interdigitated electrode arrays: analytical solution using Fourier series, J. Phys. D, Appl. Phys. 34 (10) (2001) 1553–1561.
[2] H.J. Song, D.J. Bennett, A semi-analytical approach using artificial neural network for dielectrophoresis generated by parallel electrodes, J. Electrost. 68 (1) (2010) 49–56.
[3] G. Karniadakis, A. Beskok, N. Aluru, Microflows and Nanoflows: Fundamentals and Simulations, Springer, New York, NY, 2005.
[4] J. Kadaksham, P. Singh, N. Aubry, Dynamics of electrorheological suspensions subjected to spatially nonuniform electric fields, ASME J. Fluids Eng. Trans. 126 (2) (2004) 170–179.
[5] K.H. Kang, X.C. Xuan, Y.J. Kang, D.Q. Li, Effects of dc-dielectrophoretic force on particle trajectories in microchannels, J. Appl. Phys. 99 (6) (2006).
[6] C. Rosales, K.M. Lim, Numerical comparison between Maxwell stress method and equivalent multipole approach for calculation of the dielectrophoretic force in single-cell traps, Electrophoresis 26 (11) (2005) 2057–2065.
[7] N. Aubry, P. Singh, Control of electrostatic particle–particle interactions in dielectrophoresis, Europhys. Lett. 74 (4) (2006) 623–629.
[8] P. Singh, N. Aubry, Trapping force on a finite-sized particle in a dielectrophoretic cage, Phys. Rev. E 72 (1) (2005).
[9] Y. Liu, W.K. Liu, T. Belytschko, N. Patankar, A.C. To, A. Kopacz, J.-H. Chung, Immersed electrokinetic finite element method, Int. J. Numer. Methods Eng. 71 (4) (2007) 379–405.
[10] T.B. Jones, Electromechanics of Particles, Cambridge University Press, Cambridge, 1995.
[11] X.J. Wang, X.B. Wang, P.R.C. Gascoyne, General expressions for dielectrophoretic force and electrorotational torque derived using the Maxwell stress tensor method, J. Electrost. 39 (4) (1997) 277–295.
[12] D.L. House, H.X. Luo, S.Y. Chang, Numerical study on dielectrophoretic chaining of two ellipsoidal particles, J. Colloid Interface Sci. 374 (2012) 141–149.
[13] Y. Ai, S.Z. Qian, Dc dielectrophoretic particle–particle interactions and their relative motions, J. Colloid Interface Sci. 346 (2) (2010) 448–454.
[14] A.P.S. Bhalla, R. Bale, B.E. Griffith, N.A. Patankar, Fully resolved immersed electrohydrodynamics for particle motion, electrolocation, and self-propulsion, J. Comput. Phys. 256 (2014) 88–108.
[15] T.Z. Jubery, A.S. Prabhu, M.J. Kim, P. Dutta, Modeling and simulation of nanoparticle separation through a solid-state nanopore, Electrophoresis 33 (2013) 325–333.
[16] A. Al-Jarro, J. Paul, D.W.P. Thomas, J. Crowe, N. Sawyer, F.R.A. Rose, K.M. Shakesheff, Direct calculation of Maxwell stress tensor for accurate trajectory prediction during dep for 2d and 3d structures, J. Phys. D, Appl. Phys. 40 (1) (2007) 71–77.
[17] D.V. Le, C. Rosales, B.C. Khoo, J. Peraire, Numerical design of electrical–mechanical traps, Lab Chip 8 (5) (2008) 755–763.
[18] D. Day, M.A. Heroux, Solving complex-valued linear systems via equivalent real formulations, SIAM J. Sci. Comput. 23 (2) (2001) 480–498.
[19] Z.L. Li, A fast iterative algorithm for elliptic interface problems, SIAM J. Numer. Anal. 35 (1) (1998) 230–254.
[20] R.J. Leveque, Z.L. Li, The immersed interface method for elliptic-equations with discontinuous coefficients and singular sources, SIAM J. Numer. Anal. 31 (4) (1994) 1019–1044.
[21] C.S. Peskin, Numerical analysis of blood flow in the heart, J. Comput. Phys. 25 (1977) 220–252.
[22] C.-Y. Hsu, R. Dillon, A 3d motile rod-shaped monotrichous bacterial model, Bull. Math. Biol. 71 (5) (2009) 1228–1263.
[23] R. Dillon, H.G. Othmer, A mathematical model for outgrowth and spatial patterning of the vertebrate limb bud, J. Theor. Biol. 197 (3) (1999) 295–330.
[24] O. Schenk, K. Gartner, On fast factorization pivoting methods for sparse symmetric indefinite systems, Electron. Trans. Numer. Anal. 23 (2006) 158–179.
[25] O. Schenk, A. Wachter, M. Hagemann, Matching-based preprocessing algorithms to the solution of saddle-point problems in large-scale nonconvex interior-point optimization, Comput. Optim. Appl. 36 (2–3) (2007) 321–341.
[26] D.M. McQueen, C.S. Peskin, A three-dimensional computer model of the human heart for studying cardiac fluid dynamics, Comput. Graph.-Us 34 (1) (2000) 56–60.
[27] D. Devendran, C.S. Peskin, An immersed boundary energy-based method for incompressible viscoelasticity, J. Comput. Phys. 231 (14) (2012) 4613–4642.
[28] G.H. Markx, R. Pethig, J. Rousselet, The dielectrophoretic levitation of latex beads, with reference to field-flow fractionation, J. Phys. D, Appl. Phys. 30 (17) (1997) 2470–2477.
[29] K. Horiuchi, P. Dutta, Joule heating effects in electroosmotically driven microchannel flows, Int. J. Heat Mass Transf. 47 (14–16) (2004) 3085–3095.
[30] C.H. Kua, Y.C. Lam, I. Rodriguez, C. Yang, K. Youcef-Toumi, Cell motion model for moving dielectrophoresis, Anal. Chem. 80 (2008) 5454–5461.
[31] T.Z. Jubery, S.K. Srivastava, P. Dutta, Dielectrophoretic separation of bioparticles in microdevices, Electrophoresis 35 (2014) 691–713.
[32] D.R. Carter, G.S. Beaupre, N.J. Giori, J.A. Helms, Mechanobiology of skeletal regeneration, Clin. Orthop. Relat. Res. (355) (1998) S41–S55.
[33] M.R. Hossan, R. Dillon, A.K. Roy, P. Dutta, Modeling and simulation of dielectrophoretic particle–particle interactions and assembly, J. Colloid Interface Sci. 394 (2013) 619–629.
[34] T.Z. Jubery, P. Dutta, A fast algorithm to predict cell trajectories in microdevices using dielectrophoresis, J. Numer. Heat Transf., Part A 64 (2013) 107–131.
[35] T.Z. Jubery, P. Dutta, A new design for efficient dielectrophoretic separation of cells in a microdevice, Electrophoresis 34 (2013) 643–650.